2017

Fabrication, Structure, And Transport Properties Of Alumina Nanofiber-Based Materials

William Anthony Brayer
University of Alabama at Birmingham

FABRICATION, STRUCTURE, AND TRANSPORT PROPERTIES OF ALUMINA NANOFIBER-BASED MATERIALS

by

W. ANTHONY BRAYER

ANDREI STANISHEVSKY CHAIR
ALAN W. EBERHARDT
RYOICHI KAWAI

A THESIS

Submitted to the graduate faculty of The University of Alabama at Birmingham,
in partial fulfillment of the requirements for the degree of
Master of Science

BIRMINGHAM, ALABAMA

2017

FABRICATION, STRUCTURE, AND TRANSPORT PROPERTIES OF ALUMINA NANOFIBER-BASED MATERIALS

W. ANTHONY BRAYER

PHYSICS

ABSTRACT

One of the most promising nano-materials is nanofibrous alumina (Al_2O_3) but current production methods are too slow and too inconsistent for applications outside of laboratory proof of concepts. Alumina structures were fabricated from aluminum nitrate/polyvinylpyrrolidone precursor nanofibers prepared using a novel free-surface alternating current (AC) electrospinning method. Precursor fibers were generated at the rates up to 6.4 g/h and collected as 100–300 μm thick sheets suitable for direct conversion into the nanofibrous alumina structures. A computational model of the surrounding electric field was constructed to compare to experimental observations. The effects of process conditions and annealing temperature on the nanofiber diameter, morphology, shrinking behavior and crystalline phase formation were investigated by Scanning Electron Microscopy (SEM), Fourier Transform Infrared (FTIR) spectroscopy, and X-ray diffraction (XRD). Textural properties of Al_2O_3 fibrous sheets composed of micro-/meso-porous nanocrystalline γ-alumina nanofibers with 260±90 nm diameters after the calcination at temperatures in the range from 700 ^oC to 1000 ^oC were determined from N_2 adsorption/desorption isotherms. Preliminary air permeability and apparent air flow resistance studies of single sheet and multilayer nanofibrous alumina membranes were performed and compared with other porous alumina membrane structures for possible usage in gas filtration, separation, and other applications.

DEDICATION

I dedicate this thesis to my friends and family, especially my mom and dad; my lab coworkers and my mentor.

"The important thing is not to stop questioning. Curiosity has its own reason for existence. One cannot help but be in awe when he contemplates the mysteries of eternity, of life, of the marvelous structure of reality. It is enough if one tries merely to comprehend a little of this mystery each day."- Albert Einstein

ACKNOWLEDGEMENTS

I thank my mentor, academic adviser, and laboratory comrade Professor Andrei Stanishevsky, who has helped me far and above anyone else in my academic career. I thank him for giving me an incredible opportunity to start a laboratory and its research focus from the ground up. His mentorship and guidance is truly a priceless resource.

I thank Professor Ryoichi Kawai and Professor Alan Eberhardt for graciously serving on my committee as well their indispensable feedback.

I further thank Professor Ryoichi Kawai for his many classes through graduate school and his rigorous standards he held me to. Instructors with his great passion for teaching along with his capacity and willingness for discussion are a rare minority.

I thank Jerry Sewell for his incredible work in machining the multiple custom built apparatuses; making possible all of my research.

I thank Amanda Holt for all of her help semester after semester.

I thank all of the office staff in the Department of Physics

TABLE OF CONTENTS

Page

CHAPTERS

LIST OF TABLES

Tables *Pages*

LIST OF FIGURES

Figure *Page*

CHAPTER 1

INTRODUCTION

Electrospinning is a rapidly growing technology for the manufacture of nanostructure materials, primarily composed of nanofibers. [1] The hyper-fine fibers produced by electrospinning exhibit two main properties, a very high surface to volume ratio, and a relatively defect free structure at the molecular level. This first property makes electrospun material suitable for activities requiring a high degree of physical contact, such as providing sites for chemical reactions, or the capture of small particulate material by physical entanglement e.g. filtration and fluid transport. The second, perhaps even more exciting, property should allow electrospun fibers to approach the theoretical maximum strength of the spun material, opening up the possibility of making ultra-high mechanical performance composite materials. Forecasts show that the filtration market alone will be as much as $7b by 2020. [2] Nano ceramics exemplify the characteristics sought by industry though reliable production of inorganic nanofibers remains elusive. [3] Inorganic electrospinning is a nearly uncharted research front. To date less than 700 papers have been published on the topic.

Electrospinning is the process of pumping a liquid solution through a millimeter diameter nozzle within an electric field to produce a fabric sheet of nano-scale fibers. From a simplistic view, electrostatic charging of the fluid causes charge grouping [4]. As a result, the formation of Taylor cones begins and from the peak of these cones a single fluid jet is rapidly ejected. Within the electric field the jet accelerates and thins; finally

charge repulsion results in radial splitting of the primary jet into multiple filaments. This process has three primary modes: (a) formation, where the fluid surface deforms with sufficient curvature to produce a Taylor cone; (b) stabile elongation, in which the jet accelerates fluid into a rapidly thinning filament; (c) precession, where the end of the filament begins a whipping motion until enough instability forms and the filament is ultimately broken. [5] The complex physics behind electrified fluids was explained by Taylor in the 1960's. [4] He found that it is not possible to account for the majority of electrical phenomena of a moving fluid if it is assumed the fluid is either a perfect dielectric or a perfect conductor; a seemingly simple assumption. This is because even a perfect dielectric still contains a non-zero charge density. Small as this charge density may be, small enough even to disregard bulk conduction, it will tend to the interface surface of the fluid. This miniscule charge in the presence of an electric field parallel to that charged surface will cause a tangential stress on that surface. The only force which can oppose this stress is the force of viscosity. [6]

The derivation for the tangential electric field within the material follows the assumptions that the jet is a long and slender object. Two Gaussian surfaces coaxial to the jet are places just inside and just outside of the surface of the jet. Elementary electrostatics tells us the tangential electric field is continuous across fluid interface. All of this leads to the equation for the tangential electric field inside the jet [6],

$$E - \ln\frac{1}{\chi}\left[\frac{\beta}{2}(h^2E)'' - \frac{4\pi}{\bar{\epsilon}}(h\sigma)'\right] = E_\infty \qquad (1)$$

Where E is the electric field parallel to the jet, χ^{-1} is the local aspect ratio, β is the dielectric ratio of the fluid to the spinning atmosphere, h is the radius of the jet, and σ is

the surface charge density. As the fluid jet turns conical χ simply becomes the slope of the cone. Building on the foundational work of Taylor [5], Saville further explored the "leaky dielectric model" for electrically driven fluids. [7] Saville went on to perform an in-depth investigation into the linear stability of jets in electric fields. [8] This equation strongly agrees with Saville's findings [7] as shown in Figure 1.

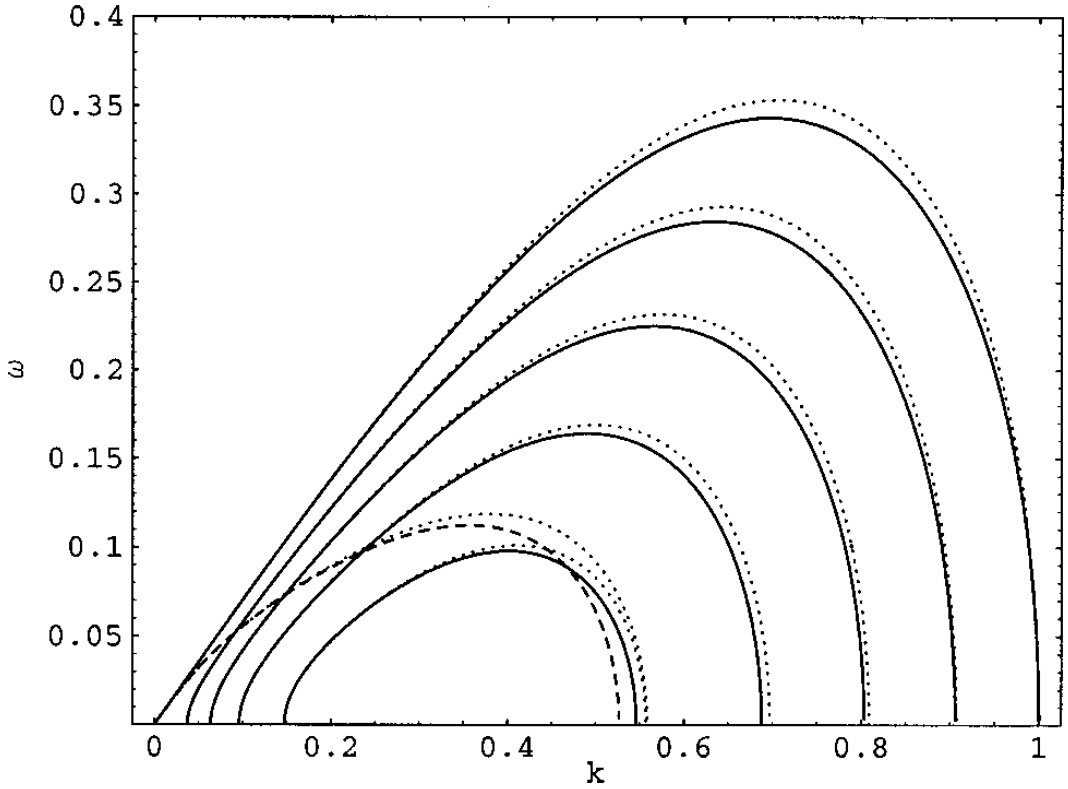

Figure 1. Comparison of Saville's findings (solid line) to the predictions of Eq. 1. The dashed line is for zero conductivity and the dotted lines are from Eq. 1 at multiple field values, where ω is jet growth rate and k is jet stability.

The above equation (Eq.1) is a simplistic approximation of the process, albeit an excellent approximation. While the tangential electric field strength has a greatest part in jet formation and stability there are other factors which play prominent roles in the process. [9] The second biggest factors in a fluids spinnability are viscosity and conductivity. [10] Great attention must be paid to a fluids conductivity so that it may be responsive to the surrounding electric field but also maintain sufficient viscosity to neither spray nor completely resist the electric force. Difficulty in achieving a balance between viscosity and conductivity emanates from their inverse relationship generally found in polymer solutions [11]. A solution with adequate conductivity will often be too thin to electrospin and rather electrospray.

Many materials, from organics and oxides to polymers and inorganics, have been successfully made using electrospinning. [1] The majority of fibers produced by the electrospinning technique is polymeric. Ceramics are the second most commonly produced material yet they only account for 3% of the total production. [12] Ceramic micro- and nanofibers are increasingly studied as material suitable for the fabrication of porous ceramic structures for demanding applications. [13 14 15 16 17 18] Most of the nanofibrous ceramic materials are currently produced from precursor fibers made by electrospinning methods [19 20 21 22] that can provide a high level of control of the fiber dimensions, shape, structure and composition. Alumina-based nanofibers have been of considerable interest due to their mechanical strength, chemical and thermal properties [23 24], and a possibility of the fabrication of stable self-supported fibrous membranes [25]. Alumina nanofibers are derived mainly from the precursor fibers prepared using the capillary needle

DC-electrospinning from various precursor solutions based on a metal salt and polymer. [26] [27] [28] [29] [30]

Aluminum Oxide (Al_2O_3), or Alumina, is an exemplary oxide ceramic with breadth of applications. Its uses span many industries as it is well suited for use in absorbents, catalysts, electrical and thermal insulators, and high temperature stable nanostructures. [31] In the last decade, Alumina based nanofibers and nanorods have gained significant attentions because of their inherent large surface area to volume ratio and well defined size. One widely implemented use of alumina, in its gamma phase, is as both a catalyst and catalyst support. [32]

Recently the growth of interest in nanotechnology has incited research on the synthesis and application of nanomaterials with a flurry of focus on inorganic metal oxides, like that of alumina. [33] [34] Ceramic structures with various levels of micro-to macro-porosity attract much attention due to a possibility to attain favorable combinations of mechanical, chemical, textural, and transport properties important for numerous applications in gas and liquid separation and filtration, biotechnology and pharmaceutical, food processing, environmental management, and catalytic processes. The final properties of these nanofibers depend on the size and homogeneity of the fibrous structure, lending to enhanced sintering ability, strength, catalytic activity, and absorption ability. [33] Many composite materials comprising of alumina nanoparticles or nanofibers as minor or major component in the presence of polymer or inorganic substrate also show similar interesting properties. [35] The preparation of the final form of alumina fiber may involve the use of polymers as an intermediate structure. Usually, the annealing of electrospun precursor fibers at temperatures between 700 °C and 1400 °C

results in micro/mesoporous nanocrystalline alumina nanofibers with diameters in the range from 100 to 500nm, specific surface area from 3.0 to 260m^2/g, and γ- or α-Al2O3 structure depending on the temperature. For example, Wang et al. [36] prepared mesoporous γ-alumina fibers with diameters 130-200nm and BET surface area up to 264.1m^2/g after calcination at 700 °C. They found that the mesopores disappear and a significant grain growth of α-alumina phase occurs after calcination of these fibers at 1100 °C.

Some major challenges in current electrospinning methods for production of ceramic fibers are: low productivity; difficulty in preparation of spinnable precursors; fiber uniformity; and control of ceramic fiber morphology and crystallinity. Attempts at higher production rates have been made from simply using more needles to more novel methods such as free surface electrospinning. [37] [38]One of the more interesting solutions to production comes from a team in the Czech Republic. Lukas et al. detail a needleless, free surface method called The Nanospider. This system consists of a long horizontal electrified wire that is continually bathed in solution. The increased surface area along with the large field concentration of a thin wire lend to the great production volume of this method. [39]

Solution preparation is a challenge in itself. The production of electrospun fibers require a finely tuned precursor solution. A proper solution must have enough polymer to produce a meaningful amount of fibers, a solvent that is volatile enough to rapidly flash off of the collected fibers so as to not dissolve the but also stable enough to be exposed to an open environment before spinning. [40] For ceramic fiber production, it further must mutually dissolve the polymer and the desired metal-salt. [41] All while maintaining the suitable parameters for conductivity and viscosity.

To go from a state polymer fibers to ceramic fibers and intermediate process must be used. The two primary processes are used to yield ceramic fibers, solvent washing and thermal processing [42]. The solvent wash method uses a bath of solvent to remove the polymer fiber, leaving behind the ceramic structure. The downside to this method is during both the electrospinning process and the wash moisture crosslinking takes place [43]. This crosslinking promotes greater ceramic production but it also causes greater fiber diameter to the point of it losing its small-scale benefits. Crosslinking in the wash also causes sites of entangled fibers and a destabilization of the micro structure produced by electrospinning [44].

Another challenge is a distinct lack of uniformity in the fibers. A useful attempt to resolve this was mad by Demir et al. [45] They found a connection between higher uniformity and increased temperature. The viscosity at 70 °C was significantly lower than at room temperature. Regrettably, Demir did not compare the spun fibers through a range of solution temperatures or even the same solution at different viscosities. A similar problem to nonuniformity is beading along the fibers. This phenomenon results in globules forming intermittently along the fibers. Fong determined that by increasing the polymer concentration the beading action was greatly reduced, however still existent. [46] An unfortunate consequence of both attempts to better homogenize fibers as well as eliminating beading is an increase in viscosity. This increase in viscosity causes as spun fibers diameter to grow, nearing the boundary of the nano/micro regime. [47] [48] [46]

Goals of Thesis

In this work, I intend to develop a method for superior alumina fiber production by electrodynamic electrospinning that is both scalable and highspeed. To achieve this,

the following major facets of material processing must be met: high-yield electrospinning process development, precursor solution optimization, collection methods, and nondestructive annealing procedures.

- Explore the feasibility of electrodynamic spinning for the high-yield generation of ceramic precursor nanofibers.
- A solution is optimized with respect to viscosity, conductivity, and concentration. While other factors are at play, albeit minorly, focus is on the most influential and least transient parameters.
- Overcoming the difficulty in consistent fiber collection. Macro fiber alignment methods used in the textile industry do not translate well into nanofibers because of their short and noncontiguous nature.
- Heat treating the fibers after production is necessary to stabilize them to the environment and afford easier handling. When performing the annealing, problems appear such as polymer shrinkage and fiber breaking can be mitigated with temperature ramp speed, soak temperature, and soak time. [49]
- Further intentions to perform a thorough characteristic investigation of nanofibrous alumina. Measurement techniques such as Scanning Electron Microscopy and X-ray Diffraction will be heavily used to determine morphological properties and crystal phase, respectively. Fourier Transform Infrared Spectroscopy is relied on to determine the evolution of sample composition through the annealing procedure and past the point of calcination.
- Evaluate the transport and mechanical properties of fabricated nanofibrous alumina for the potential applications.

CHAPTER 2

RESEARCH METHODOLOGY IN ALUMINA NANOFIBER SYNTHESIS

2.1. Precursor preparation and characterization

Aluminum nitrate nonahydrate ($Al(NO_3)_3 \cdot 9H_2O$ from Sigma Aldrich) and polyvinylpyrrolidone (PVP, M_w 1,300,000, Sigma Aldrich) were used to prepare a precursor solution for electrospinning. The salt and polymer were dissolved in DI water and ethanol, respectively, and the solutions were mixed to obtain the salt-to-polymer ratios in a range from 0.5:1.0 to 2.0:1.0 in a base precursor with 10 wt% of polymer. The base precursor was then diluted with either ethanol or water to vary the concentration and solvent composition. The precursors were stirred for up to 24 h using a magnetic stirrer and stored at normal laboratory conditions.

Viscosity of $Al(NO_3)_3$/PVP precursor solutions was determined using a HAAKE RotoVisco 1 from Thermo Scientific paired with Rheowin 4 Job and Data Manager Software. The RotoVisco was programmed to calibrate the zero point before each sample test. Once calibrated a drop of the solution was placed on the RotoVisco platform, and the viscosity values were recorded over a 120-second time period at 1000 rpm. The viscosity graphs and recorded values were stored within the Rheowin 4 Data Manager and could be exported for further analysis.

Electrical conductivity was measured using the WTW inoLab pH/Cond 720 instrument. The meter was calibrated according to the WTW inoLab 720 instruction

manual. The AutoRead function was used to obtain at least 5 stabilized values for each sample.

2.2. Dynamic electrospinning procedure

Electrospinning of $Al(NO_3)_3$/PVP precursor nanofibers was carried out using two similar alternating current systems capable of producing AC-voltages up to 40 kV rms and operated either at 60 Hz or 50 Hz. [50 51] Initial observation of the precursor spinnability was done by placing a small amount of precursor solution on circular electrodes (Fig. 2) with different diameters (6–25 mm) and applying AC-voltage (15–40 kV rms). The formation of a stable flow of fibers served as major criterion for the selection of the precursor for further experiments. All stages of the fiber generation were recorded at 2000 fps using an Olympus i-speed series camera as well as other photo- and video-recording equipment. Spinnable precursor solutions were loaded in an electrically insulated line equipped with a pump, and delivered through the base of electrode to its surface. Generated fibers were collected either on a flat sheet of paper, plastic mesh, or rotating plastic cylinder. A grounded collector was not used.

The formation of a dense flow of $Al(NO_3)_3$/PVP precursor fibers in the AC-electrospinning process is presented in Figure 3. When an alternating electric field is applied to a layer of viscous polymer solution, it leads to the formation of a pulsating pattern of protrusions along the electrode's circumference during a few initial high voltage oscillations (20-80 ms) (Fig. 3a, insert). Next, the jets develop from those protrusions (Fig.3a) thus starting the fibrous flow (Fig. 3b). Once the jets are initiated, in the case of $Al(NO_3)_3$/PVP precursor the liquid layer quickly relaxes back to its initial

shape, while multiple jets continue to generate randomly from the entire surface of the polymer solution quickly forming a fibrous cloud above the electrode surface (Fig. 3c) accompanied by the charge recombination at its external boundary. Next, the fibrous mass is pushed upwards by ionic wind [52 50], which results in a flow of solidified polymer fibers with a low residual electric charge (Fig. 3d,e) propagating toward the collector located at 300–350 mm distance from the fiber generating electrode (Fig.3f). The average speed of propagating flow of $Al(NO_3)_3$/PVP precursor fibers was in the range 0.2–0.4 m/s and slightly dependent on the applied voltage.

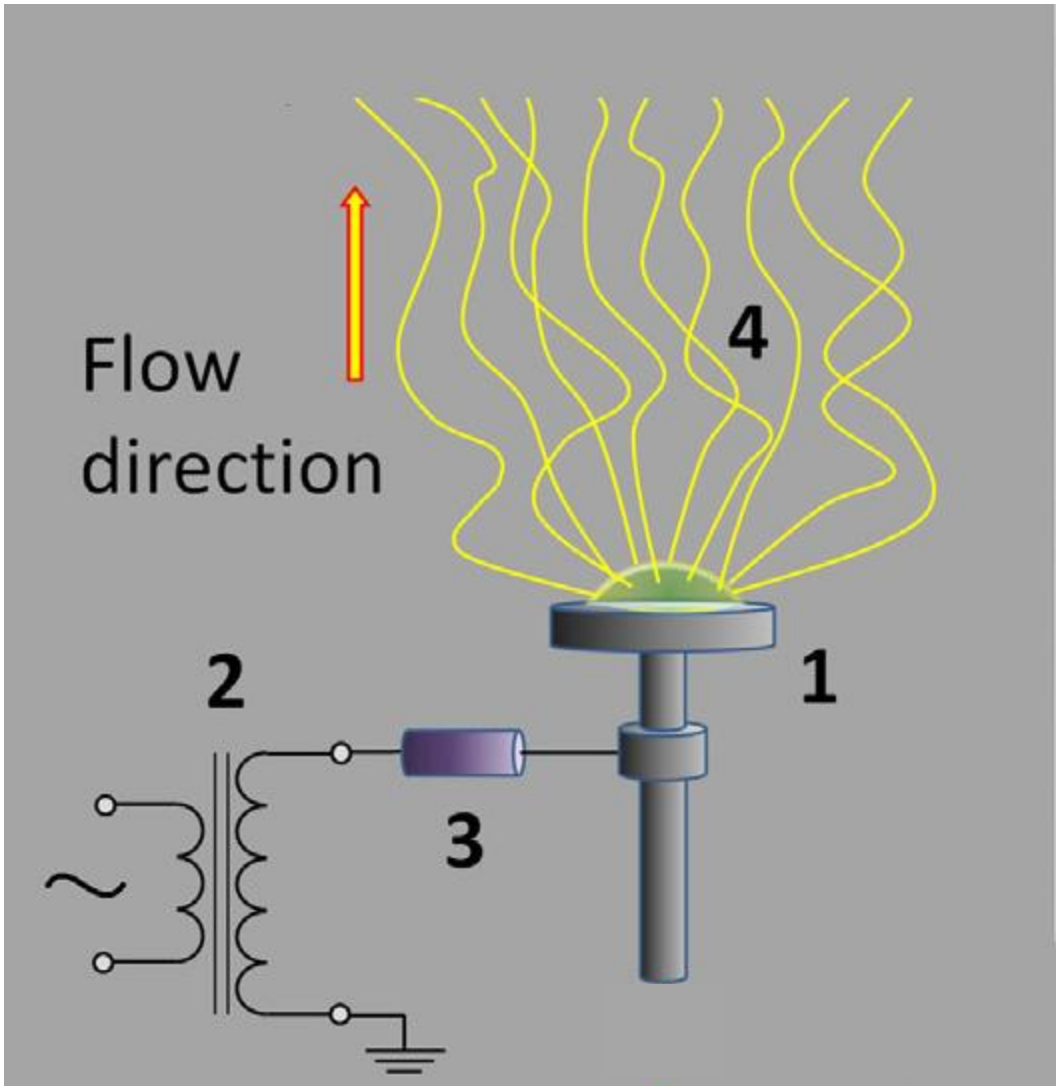

Figure 2.Proccess schematic. The precursor solution is placed on the electrode (1) that is connected to a grounded high-voltage transformer (2), through a current- limiting resistor (3). Electrified jets are generated from a layer of precursor and form flow of fibers (4) that are collected.

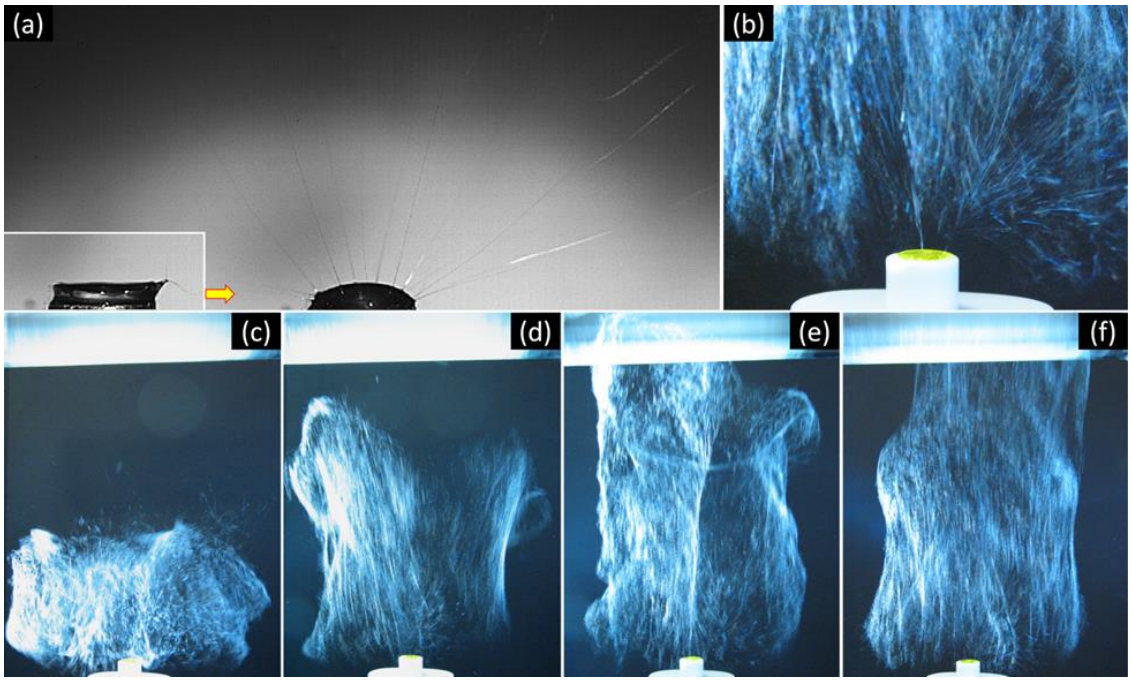

Figure 3. Highspeed photographs. (a)High-speed video shots (2000fps) of a layer of precursor solution on the 8-mm diameter electrode at the jet initiation(insert) and development stage; (b)close up photo (12mm diameter electrode) of the polymer jets emitting from Al(NO3)3/PVP precursor during the AC-electrospinning at 25kV rms voltage; (c–f) various stages in the development of the fibrous flow propagating towards a rotating collector.

2.3. Thermal processing of precursor nanofibers

As prepared Al(NO3)3/PVP precursor nanofibers were normally removed from the support in a form of fibrous sheets with a thickness in a range from 100 to 300 μm and dried in an oven at 80–120 ^{o}C to eliminate the residual solvent and stabilize the material. Fibrous sheets were then cut in pieces (typically 75×25 mm) and assembled into constructs made of up to 10-sheets. Some single and multi-sheet constructs were compressed for 300 seconds at up to 100 kPa pressure applied normal to their surface and then placed between two alumina or quartz plates to maintain their shape during the thermal processing. Next, the precursor nanofibers and fibrous sheets were calcined in air at temperatures ranging from 500 ^{o}C to 1000 oC for 2 hours using a programmable furnace (Isotemp from Fisher Scientific, heating rate 3 °C/min used).

2.4. Analytical techniques

A myriad of analytical techniques were used to conduct this study. Microscopic, spectroscopic, and mechanical property measurement methods were relied on to form a complete picture of this highly complex system. Scanning Electron Microscopy is well suited for determining morphology and structure of nanoscale fibers. SEM provides image resolution well below the fiber size with a depth of field far superior to that of optical microscopes [53]. When dealing with fiber diameters of half to a quarter the wavelength of visible light optical systems fall short. Such great resolution allows simple dimension measurements that are incredibly accurate. [54] Unfortunately SEM cannot

determine the crystal structure of materials; for this X-Ray Diffraction is an indispensable tool. XRD is a technique used for determining the atomic and molecular structure of a crystal, in which the crystalline atoms cause a beam of incident X-rays to diffract into many specific directions. By measuring the angles and intensities of these diffracted beams, a 3-dimensional picture of the density of electrons within the crystal can be made. From this electron density, the mean positions of the atoms in the crystal can be determined, as well as various other information. A key characterization that can be made is the crystalline phase and grain size of a sample, provided the grains are smaller than about 30nm. [55] To gather further chemical bond information Fourier Transform Infrared Spectroscopy is used. FTIR is an absorption spectroscopy and like any absorption spectroscopy the technique centers on measuring how much light of a given wavelength is absorbed by a sample. [56] FTIR extends this principle by shinning multiple wavelengths simultaneously and measuring the absorption. Then a different set of frequencies is used and the absorption is measured again; this process continues many times. [57] Using the absorption energy one is able to determine vibrational frequencies and therefore chemical bond information. Tensile strength measurements were acquired using a straightforward approach. Strength is the amount of force a material can stand while still returning to its original shape, so called elastic deformation. [58] When a tension force is applied to any material it will deform and resist. Fixing on end of a sample to a force meter and the other to a micrometer resolution moving stage allows precise tension, stress measurement while simultaneously knowing the current deflection, strain. Using these values Young's modulus can be calculated as the slope of stress to strain. This can be extended to quantify the maximum load a material can endure before it catastrophically fails. [59]

CHAPTER 3

ELECTRODYNAMIC SPINNING

Most of the nanofiber research reported so far has been on nanofibers made at DC-potential. The whipping of polymer jets in DC-electrospinning, along with poorly controlled residual electric charge in solidified fibers has led to rather complicated design of equipment in the attempts to achieve the desired nanofiber structures. Nevertheless, there is a small handful of reports on another electrospinning method that caught our attention due its potential to reduce the whipping and residual charge effects while increasing the fiber generation rate and controllability. This method, that is referred here as "electrodynamic spinning" utilizes an alternating current electric field for electrospinning, which brings in additional tunable parameters and new interesting features to process. It has been demonstrated that the whipping instability of the propagating electrified jets can be overcome by applying an AC-potential that induces short segments of alternating polarity, thereby reducing the magnitude of the destabilizing force on the fiber.[60 61 62 63] Two effects were noted in this method. First, the liquid jet was oscillating, which was responsible for the smaller linear portion in the jet. Second, there could be multiple jets emerging out from the meniscus, producing fibers every half cycle. Additionally, the presence of both positive and negative segments in the fiber resulted in increased stabilization and alignment of the resultant fibers since charge repulsion effects were reduced as compared to DC-electrospinning. This led to a huge

enhancement of fiber generation. Yet, there are no models of the fiber generation and propagation in this process.

Unlike traditional needle spinning methods a flat electrode was used to facilitate the electrospinning. From experimental observations, it was found that small changes to dimension or geometry had a tremendous effect on the electrodynamic spinning process. The fiber flow ranged from highly dispersed to tightly confined and its stability can be anywhere from nonexistent to nearly steady state. Clearly, understanding the intricacies of electrodynamic spinning require an intimate grasp of the electrode's roll. The only reasonable way to study how the subtle differences in shape from one electrode to another effects the electric field is through modeling.

The electrode that was used to create the fibers was digitally modeled in COMSOL Multiphysics. The Electrostatics package within the AC-Module was used for all calculations. The electrode itself is a "T" of revolution shape made from aluminum. Conveniently the cylindrical symmetry allows for boundary condition solutions rather than brute-force solving methods. To further optimize computational resources this geometry was projected into 2-dimensions. Good optimization made it possible to have a highly-detailed model mesh, making for far greater resolution in field calculation and therefor accuracy.

The construction of the model began with a physically accurate depiction of the electrode (Fig. 4) along with all the material properties associated with it (e.g. conductivity, permittivity, ect.). Surrounding the electrode is an atmosphere of air which is a circular shape with a radius of 3 meters. The outer edge boundary of this atmosphere is treated as with a boundary condition such that there is no potential beyond this point,

r > 3m. This relatively small “universe” was chosen for its symmetry and its small size to increase the mesh density around the electrode.

A potential of 28 kV was placed in the electrode and the outer boundary of the atmosphere was set as ground. Boundary layer conditions were set at the interface of the electrode surface and the atmosphere. These were used in attempt to reduce anomalies present in the mesh at this boundary. A problem arose where the model would blend the electrode-air boundary and merge the materials, resulting in a quasi-air/aluminum material. Another oddity the figure (Fig. 5) shows is an electric field present in the electrode. This is a consequence of a geometric mesh with points straddling the air-aluminum boundary. Obviously for any conductor the electric field inside should be zero.

The model in Figure 5 shows great agreement with the experimental observations made using highspeed photography (Fig. 6). The electric field lines are show leaving the top surface nearly tangential at the center and subsequent field lines bend further as the move away from the center. It can also be seen that the density of field lines decrease at the edges and side of the electrodes top. Interestingly there is a high field density coming off the diagonals of the underside of the electrode. During the electrodynamic spinning process fibers will occasionally cross into this area of dense field lines and become vigorously accelerated away from the rest of the fiber flow. As shown in Figure 2 the precursor solution is only on the top of the electrode. This causes its primary interaction to be with the top surface electric field.

When comparing the images of spinning fibers to the model it can be seen (Fig. 6) that the fibers strongly follow along the electric field lines (Fig. 5). This is the exact behavior predicted by Hohman et al in Equation 1. Experimental, computational, and

theoretical data strongly agree with one another as seen when comparing the two figure (5 and 6). The fibers can be seen curving upward from the edges just as the model shows. Additionally, the underside is devoid of fibers and the greatest density of fibers is in the center top region; again just as the model predicted.

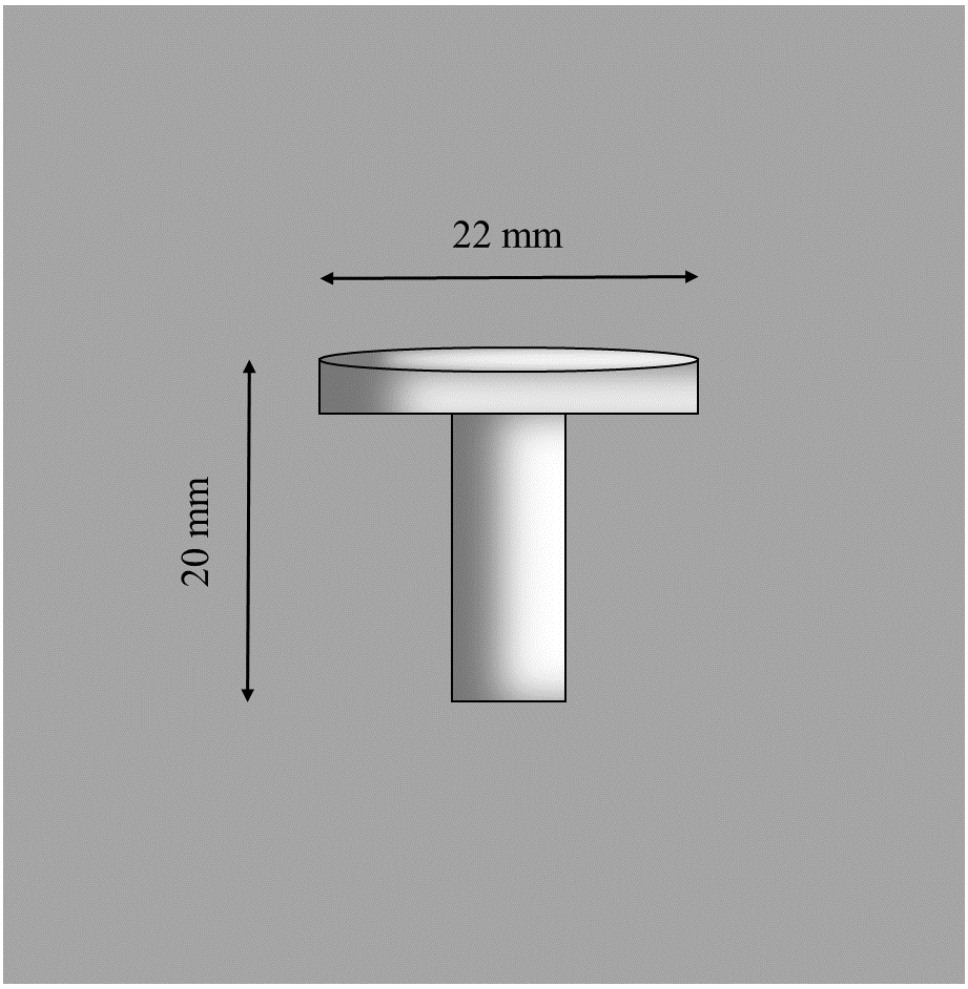

Figure 4. Electrode schematic. A schematic of the dimensions of the "T" of revolution electrode.

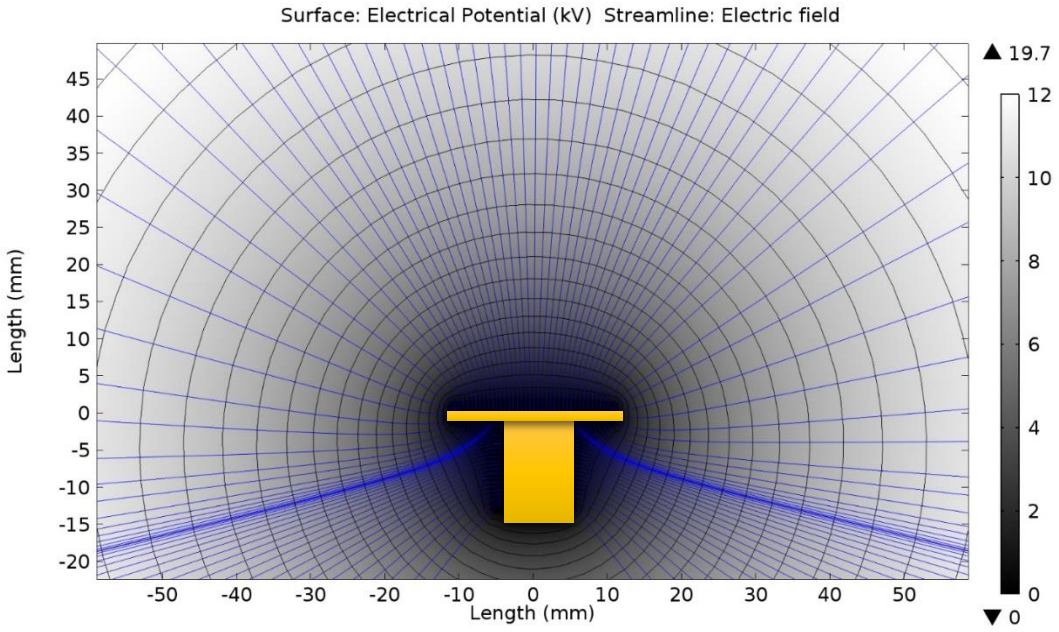

Figure 5. Electric field model. Plot of the computed potential in gray gradient with equipotential lines every 1000 V. The blue lines show electric field lines emanating off of the electrode surface.

Figure 6. Highspeed electrode comparison. A frame taken from highspeed video of the electrodynamic spinning process. The video was recorded at 2,000 frames per second.

CHAPTER 4

CRYSTALLIZATION AND STRUCTURE OF ALUMINA NANOFIBERS

It has been noted earlier that when spun from the same precursor, the diameter and shape of fibers generated in the AC-electrospinning process can differ from those of fibers prepared by other electrospinning methods.[51 64] Stable AC-electrospinning in the case of $Al(NO_3)_3$/PVP fibers was achieved with the precursor solution in ethanol containing up to 30 v% of water when the solution viscosity was in the range from 50 to 110 mPa·s. The precursor flow rates in present experiments were varied in the range from 15 to 40 mL/h that allowed the fibrous mass collection rate up to 6.4 g/h. The representative SEM images of the precursor fibers with $Al(NO_3)_3$/PVP 1:1 mass ratio prepared at different AC-voltages are shown in Figure 7(a-c). Annealing of the precursor fibers in air at temperatures up to 1000 ^oC led to a drastic reduction in the volume and mass of the material while little changes were observed in the shape and surface morphology of fibers (Fig. 7b and c).

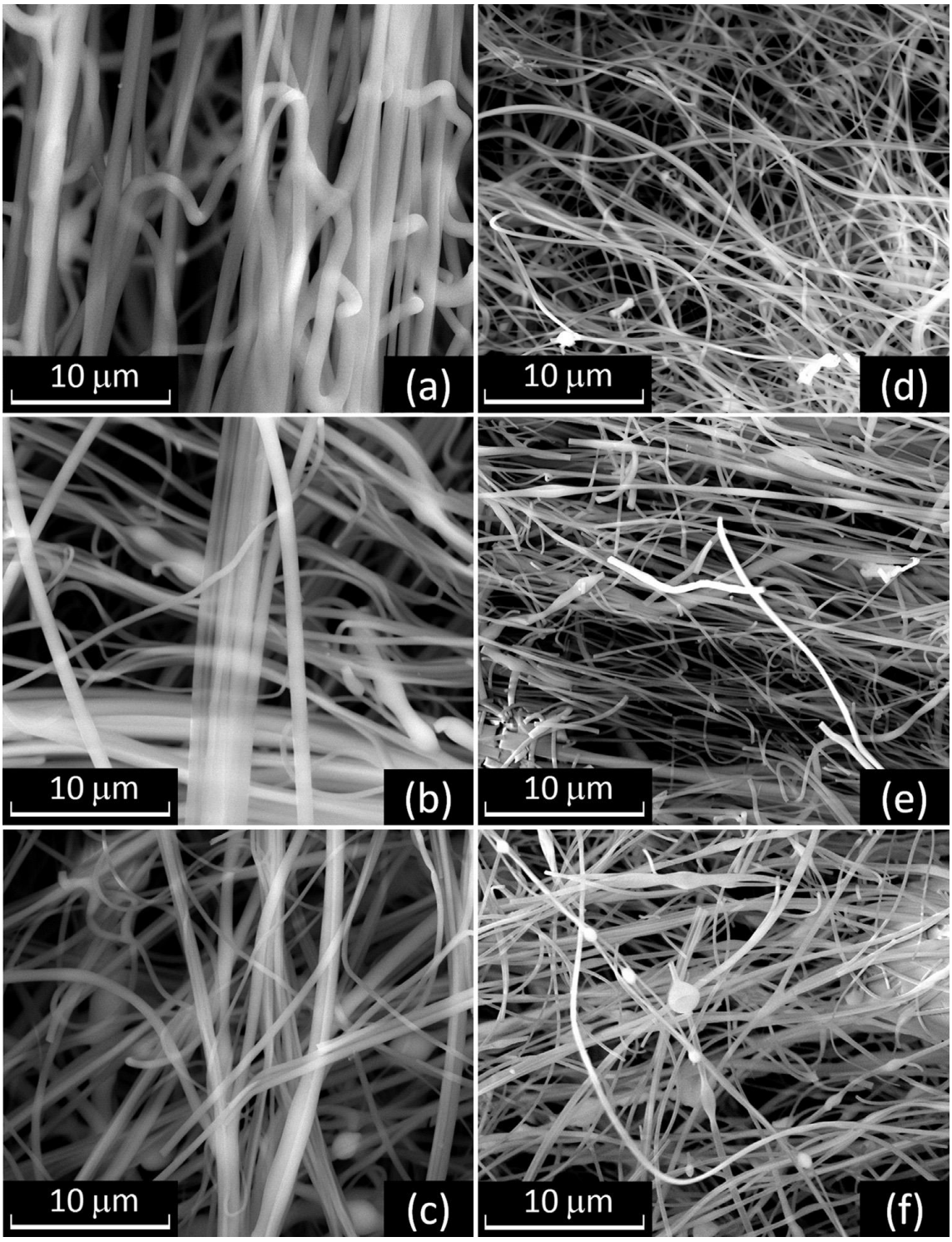

Figure 7. SEM of fibers. Representative SEM images of AC-electrospun(a–c) precursor Al(NO3)3/PVP fibers, and (d-f) fibers after the annealing for 2h at 1000 °C

The size, shape, and surface morphology of the precursor and alumina nanofibers were investigated by field-emission scanning electron microscopy (FE-SEM, FEI Quanta 450). SEM imaging was done in secondary electron mode, with an accelerating voltage of 15 kV, electron probe current 2 μA, and a chamber pressure of 1×10–4 Pa.

It was observed that the diameter of $Al(NO_3)_3$/PVP precursor fibers decreases with the increase of AC-voltage. On average, the diameter reduced from 850±250 nm to 470±200 nm when the voltage changed from 19 kV to 31 kV. The least spread of fiber diameters was achieved at 25–28 kV rms AC-voltages. The diameters of fibers shrunk down to 200–300 nm after the annealing procedure. The observed trends in fiber diameters generated at different AC-voltages and annealed at 500, 700, and 1000 ^oC are summarized in Figure 8. Interestingly, there was statistically insignificant variation in the diameters of calcined fibers, although their initial diameters varied substantially depending on the AC-voltage. For example, the diameter of precursor fibers prepared at 19, 25, and 31 kV reduced 2.5, 1.7 and 1.5 times, respectively, after the calcination at 500 ^oC. One possible explanation of this fact is the voltage dependency of the organization of PVP molecules in the fiber that results in molecular stress in it. When the fiber is heated, the stress is relieved leading to fiber shrinkage. If the fibers prepared at higher voltage are more stressed along their axis, it is possible they shrink more along their length than radially. Thus, most of $Al(NO_3)_3$/PVP fiber shrinkage should occur at relatively low temperature before the polymer matrix starts to degrade. Once the polymer component is decomposed (below 500 ^oC), further fiber shrinkage (1.1–1.4 times) at 700 ^oC and 1000 ^oC is associated with the crystallization and phase transformations of inorganic component.

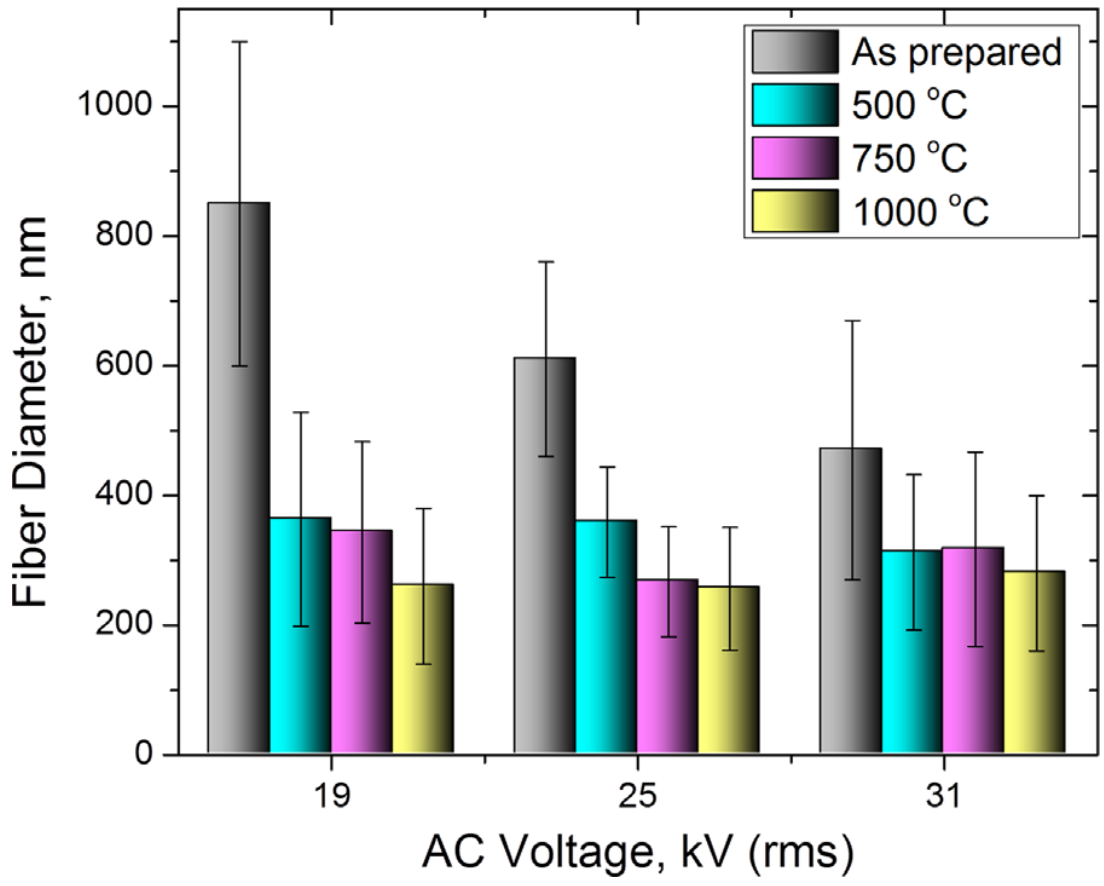

Figure 8. Diameter comparison graph. The effect of AC voltage on the diameter of the Al(NO3)3/PVP precursor and annealed alumina fibers.

FTIR spectra (Vertex 70 spectrometer, Bruker Optics) were acquired in transmission mode from the nanofiber sheets positioned in the focal point of the IR beam path. In all cases, the FTIR spectra represented an average of 32 scans recorded with a resolution of 4 cm^{-1} for each sample.

FTIR spectroscopy (Fig. 9) revealed that the PVP spectrum changes a little in $Al(NO_3)_3$/PVP precursor nanofibers dried at 120–140 ºC due to an overlap with aluminum nitrate absorption peaks at ~1360 cm^{-1} ($–NO_3$) and 1650 cm^{-1} (–OH) groups [65], and all the characteristic IR features of the precursor fibers disappear after calcination at 500 ºC. A broad asymmetric absorption band forms in the range from 500 to 1000 cm^{-1} at that temperature and it is associated with the formation of alumina. However, the material remained X-ray amorphous and did not produce any XRD pattern. A weak absorption band observed around 1500–1600 cm^{-1} is due to the carbonized residue. This band becomes weaker in the spectrum of 700 ºC calcined material, and it completely disappears in the spectrum of 1000 ºC calcined fibers. Both 700 ºC and 1000 ºC calcined alumina fibers show also a very weak but sharp 2340 cm^{-1} peak of CO_2 adsorbed due to the increased micro-/mesoporosity in the calcined material as will be shown further in the text.

Crystalline phase composition of the formed alumina nanofibers was determined using a Philips X'pert MPD thin-film X-ray diffractometer with a Cu Kα tube (wavelength 0.15406 nm) operating at 45 kV and 40 mA. The detector was scanned between 20º and 70º, with a constant take off angle of 5º. The experimental diffraction patterns were compared with the ICDD powder diffraction file (PDF) database. [66] The size of Al2O3 crystallites was estimated using Scherrer equation. [67]

The broad absorption band in the range from 500 to 1000 cm^{-1} in 700 ^{o}C calcined nanofibrous alumina resembles the profile of such band reported for γ-alumina [68]. XRD pattern of this material shows three weak and broad maxima (Fig. 10) corresponding to (222), (400), and (440) reflections of γ-Al_2O_3 with the calculated crystallite size 6±1 nm. FTIR spectrum of 1000 ^{o}C calcined sample indicates further evolution of Al-O absorption bands where the main band around 512 cm^{-1} can be fitted with two peaks centered at 544 and 486 cm^{-1}. A small sharp peak can be noted at 728 cm^{-1} along with a better defined broad absorption bands around 660 and 830 cm^{-1}. These changes can be indicative to transitional alumina phases or α-alumina [69 70 71]. XRD pattern of 1000 ^{o}C calcined fibers is still dominated by the reflections of γ-alumina phase with the calculated crystallite size 11±1 nm. A new peak at $2\theta=25.5^{o}$ can be assigned to reflection of a-alumina phase with the calculated crystallite size 17±1 nm, but other characteristic peaks of α-alumina are absent. The formation of α-Al_2O_3 has yet to be verified in this case, although the transition from γ- to α-alumina phase has been observed at 1000 ^{o}C in alumina fibers formed from various electrospun precursors. [69 31 72]

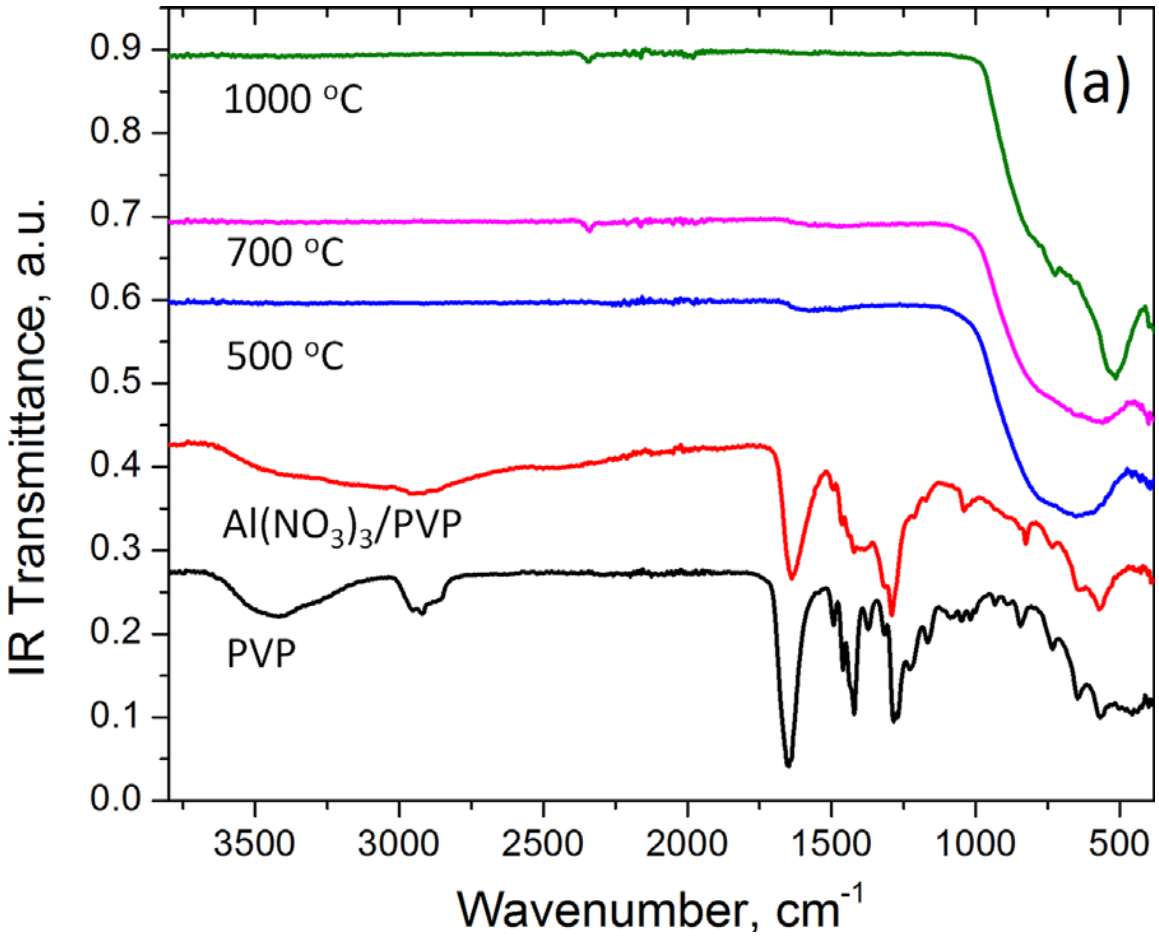

Figure 9. FTIR of fibers.FTIR spectra of the precursor Al(NO3)3/PVP and calcined alumina fibers.

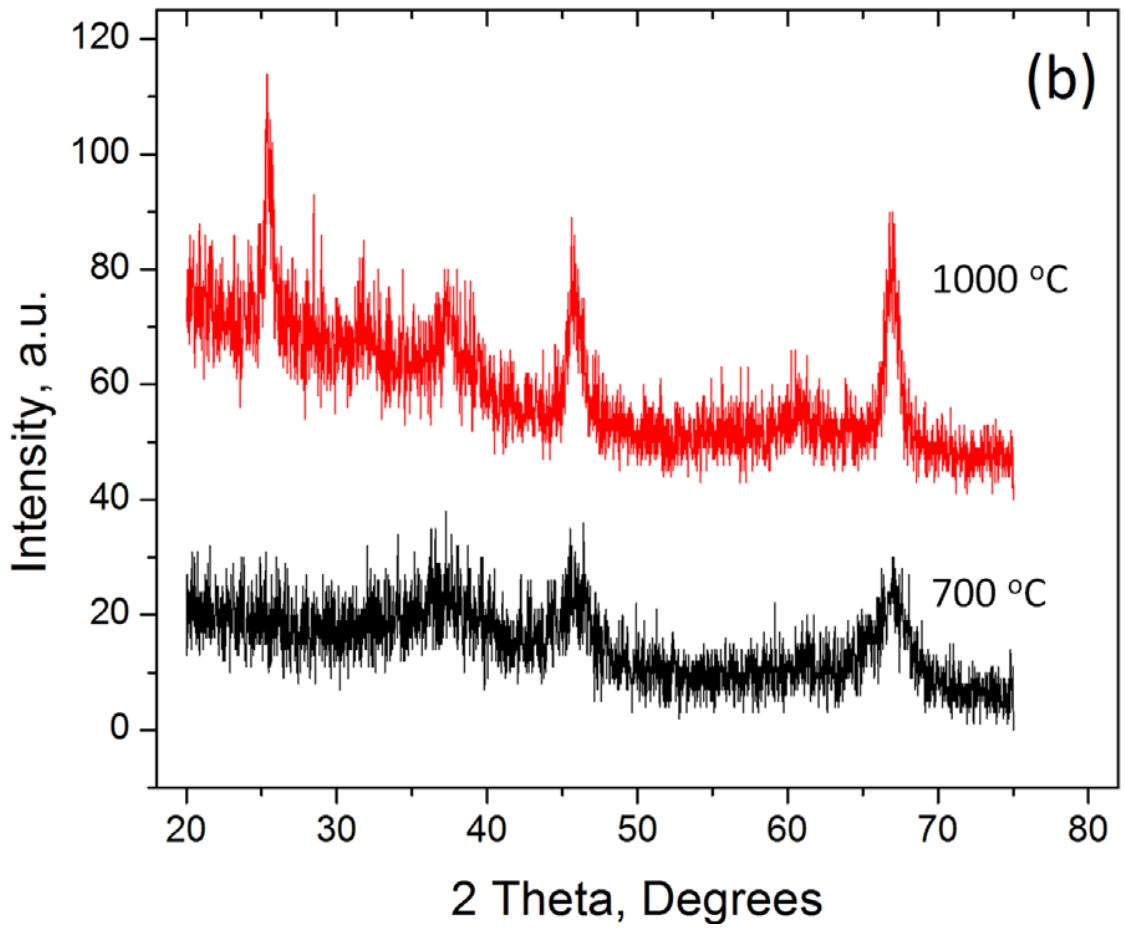

Figure 10. XRD of fibers. XRD patterns of crystallized fibers sintered at 700 °C and 1000 °C.

CHAPTER 5

TRANSPORT AND MECHANICAL PROPERTIES

Figure 11 presents the results on the fabrication of nanofibrous alumina structures from the 25-kV rms AC-electrospun 1:1 $Al(NO_3)_3$/PVP precursor fiber sheets with 80–200 μm thickness (Fig. 12a). Fibrous alumina constructs were formed from the multilayer assemblies of precursor fiber sheets (e.g., 75×25 mm pieces and up 10 layers thick, Fig.12b) that were calcined at 700 ^oC (Fig. 12c) and 1000 ^oC (d,e), according to the procedure described in the methods section. Visual and light microscopy examination indicated little warping and lack of cracking in the calcined structures. The nanofibrous sheets shrunk 2.4–2.8 times after sintering at 700 ^oC for the lateral dimensions regardless the number of layers in the assembly. Concurrently, the thickness reduced typically 1.45–1.55 and 2.4–2.5 times for a single sheet and multilayer (7 sheets in this experiment) assembly, respectively. There was a little (~10%) further shrinkage in each direction observed after calcination at 1000 ^oC. The corresponding volume shrinkage of was as large as 11–15 times and 18–25 times after calcination at 1000 ^oC for the single nanofibrous alumina sheet and 7-sheet assembly, respectively.

In the used precursor-fibrous material, nanofibers are packed mostly horizontally in a plane of individual sheet with a certain fraction of fibers present at the sheet surface (Fig. 12f). These rather loose surface fibers have fewer contact points where they can clamp and fuse to each other during the compression and sintering, when compared to the bulk of the sheet. This can cause some anisotropy in the shrinking behavior of nanofibers

across and along the fibrous sheet [64]. The role of loose surface fibers is therefore predicted to diminish in thicker or multilayer sheets that can lead to more uniform volume shrinkage and the formation of denser fibrous structures (Fig. 12g). The observed shrinkage of the fibrous sheets correlates with the magnitude of changes in the dimensions of individual nanofibers (Fig. 12h). The resulting apparent mass density of the fibrous alumina sheets was 0.18–0.22 g/cm^3 and 0.26–0.28 g/cm^3 after calcination at 700 ^{o}C and 1000 ^{o}C, respectively. It should be noted that the density of single nanofibrous alumina sheets was somewhat lower (~20%) than that of multilayer sheets. This was consistent with the difference in volume reduction of single sheet and multilayer assemblies during the sintering.

Textural properties of alumina nanofibers were determined using the Micromeritics® ASAP 2020 automatic physisorption analyzer. The Brunauer, Emmett, Teller (BET) surface area was calculated from isothermal adsorption of N2 at 77K. Barrett-Joyner-Halenda (BJH) analysis was used for pore volume and pore size distribution, and microporosity information was inferred through the t-plot analysis.

The analysis of nitrogen adsorption-desorption isotherms acquired for the 700 ^{o}C and 1000 ^{o}C calcined nanofibrous alumina sheets indicated the presence of both micro- and mesopores in nanofibers. Some structural and textural characteristics of these materials are given in Table 1. Micropores were found as a dominating pore fraction (76.0% of total pore volume) in the fibers calcined at 700 ^{o}C, and mesopores dominated in fibers calcined at 1000 ^{o}C (micropore fraction was only 20.7% of total pore volume). Quite unexpectedly, the BET surface area was nearly the same in both materials. These numbers are 5–10 times lower than the magnitude of specific surface area usually

reported for electrospun loose alumina nanofibers [36 69 73], but somewhat similar to that of electrospun commercial γ-alumina nanofibers as measured by Saunders et al [74] and γ-alumina membranes made from electrospun fibers. [25] The observed textural characteristics can possibly be associated with a denser fiber structure achieved due to the selected sintering procedure and the composition of the precursor fibers. It has been suggested that the fibers calcined at 700 ^{o}C could contain closed micropores that do not contribute to the measured numbers of the surface area and micropore volume. Furthermore, the fiber-to-fiber interaction due to the fiber bundling in the propagating fibrous flow during the AC-electrospinning and additional fiber clamping during the sheet compression can contribute towards the reduction of the surface area. The fibers densify further during the calcination at 1000 ^{o}C and exhibit the grain growth. The volume of open and closed micropores declines through the formation of more mesopores, which leads to a much larger total pore volume while keeping the specific surface area nearly the same.

Preliminary data from tensile tests (Fig. 13) indicates that the tensile modulus is low (63 MPa), for the measured bulk porosity of the fabricated materials ~0.2 g/cm^3. Assuming the theoretical relationship between the modulus and density of porous and bulk materials in a case of a random nanofibrous mats [75], $(E_{por}/E_{bulk}) = (\rho_{por}/\rho_{bulk})^2$, this gives the magnitude of E_{bulk} ~ 50 GPa, which is a reasonable number for a microporous material annealed at 700 °C. Figure 14 shows the tensile testing for the same material annealed at 900 °C. The tensile modulus is 234 MPa, which gives in theory ~355 GPa for the corresponding bulk material (very close to 375 GPa modulus of alumina ceramics with 99.5% density.

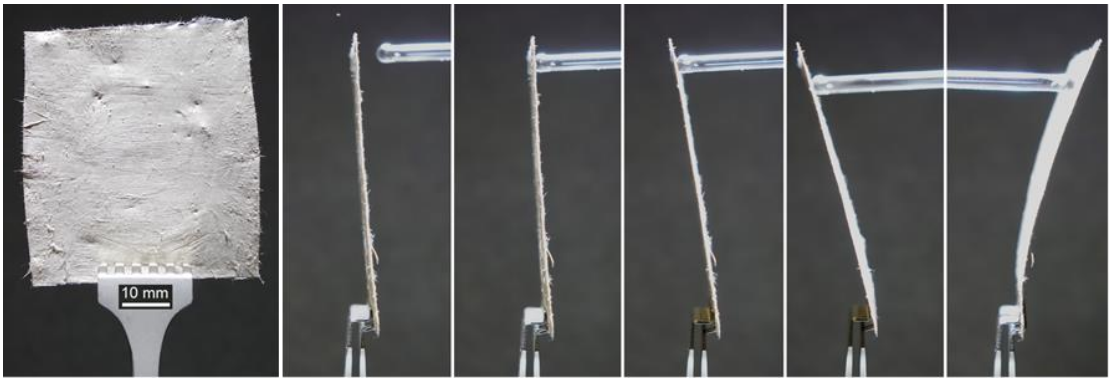

Figure 11. Flexibility of material. Single layer γ-Al_2O_3 nanofibrous sheet calcined at 700 °C for 4 hours. The sheet is able to be repeatedly bent in both directions without breaking or showing fatigue

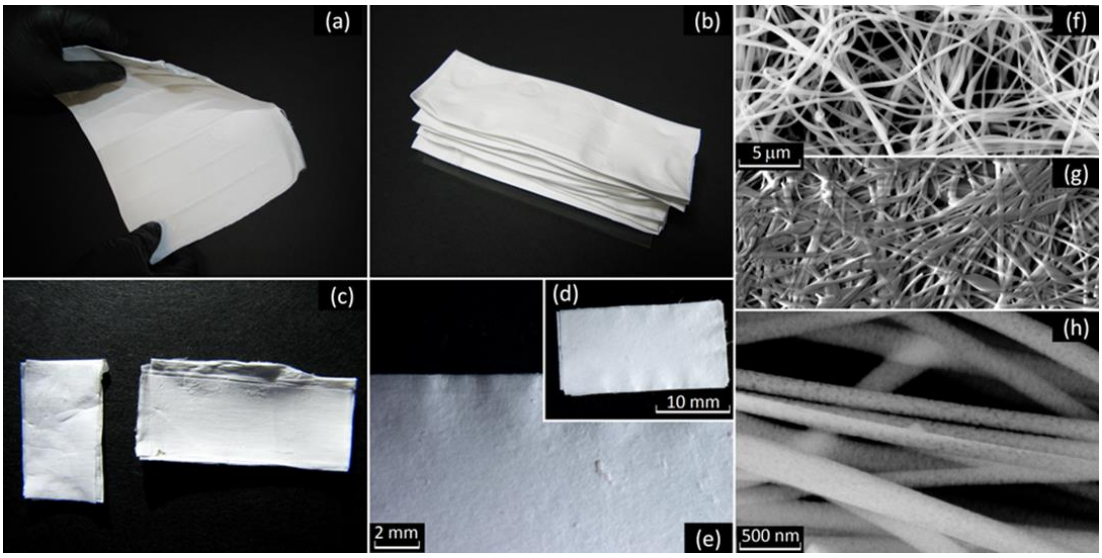

Figure 12. Stacked sheets. Fabrication of fibrous alumina constructs:(a) as prepared ~300mm ~210 mm sheet, (b)multi-sheet assembly of Al(NO3)3/PVP precursor nanofibers, and multi-sheet alumina constructs sintered at(c)700 °C and (d,e)1000 °C; SEM images of sintered at1000 °C (f)non-compressed and (g)compressed fibrous alumina single sheet and (h) individual alumina nanofibers.

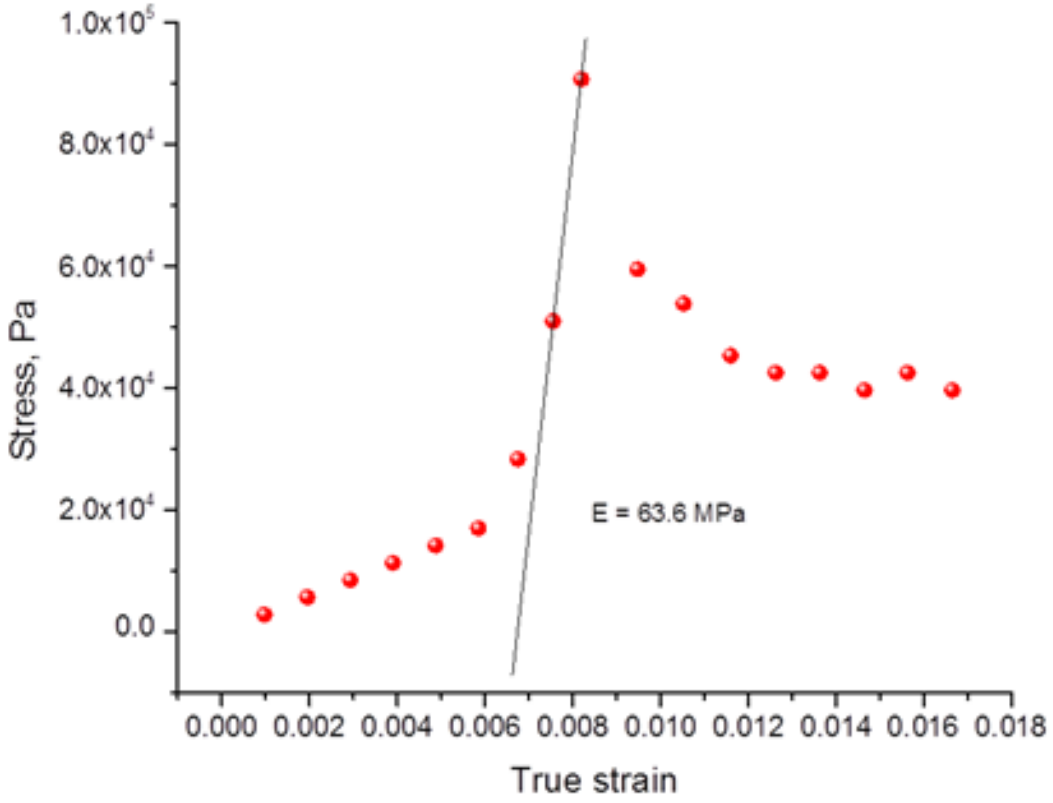

Figure 13. Strain vs. Stress 700°C. Strain vs. stress of γ-Al_2O_3 nanofibrous sheet calcined at 700 °C for 4 hours.

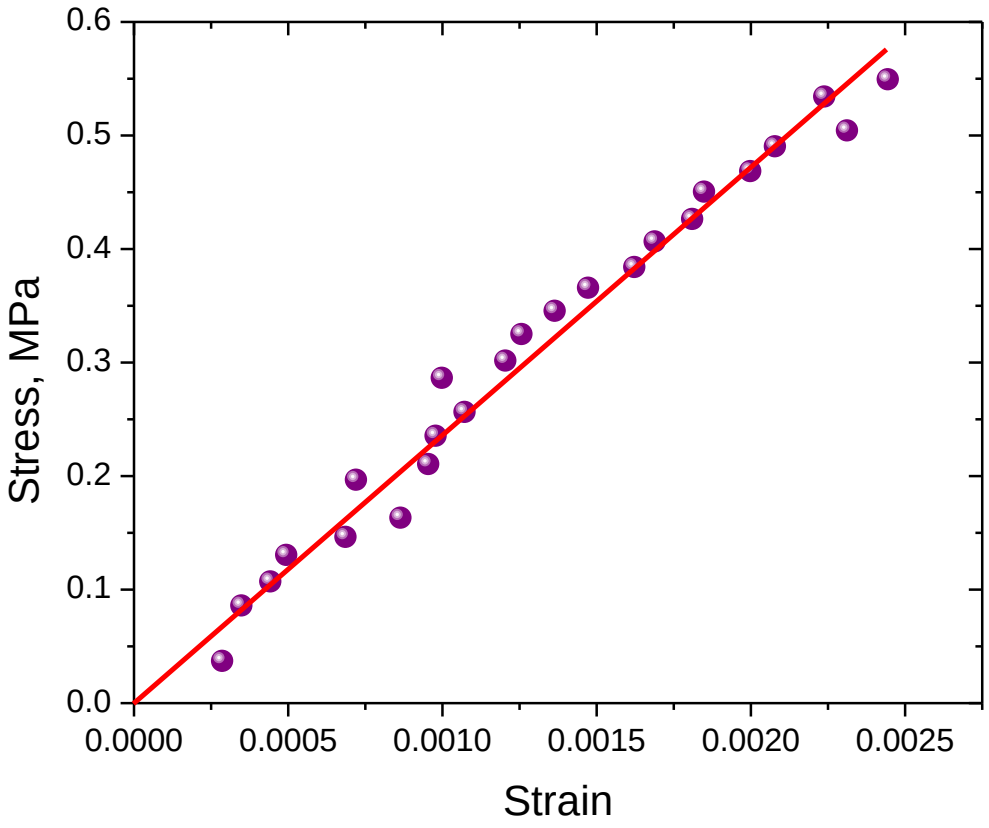

Figure 14. Strain vs Stress 900°C. γ-δ-α intermediate phase Al2O3 nanofibers annealed at 900 oC (mass density 0.094 g/cm3). The tensile modulus is 234 MPa, which gives in theory ~355 GPa for the corresponding bulk material (very close to 375 GPa modulus of alumina ceramics with 99.5% density

Table 1. Alumina sheets sintered at different temperatures. Structural and textural characteristics of nanofibrous alumina sheets sintered at 700 °C and 1000 °C.

Sample	**Fiber diameter, nm**	**Grain size, nm**	**Apparent mass density, g/cm^3**	**BET surface area, m^2/g**	**Total pore volume, cm^3/g**	**t-plot micropore volume, m^3/g**	**BET$_{(4V/A)}$ pore width, nm**	**BJH ads. / desorp. pore diameter, nm**
700 °C	267±85	6.0±1.0	0.200	13.6	0.0075	0.0057	2.20	27.4/13.9
1000 °C	256±95	14.0±3.0	0.275	14.7	0.0237	0.0049	6.45	17.1/6.9

Fibrous alumina sheets calcined at different temperatures were also evaluated for potential applications as porous ceramic membranes or filters using a custom membrane capillary flow test cell similar to those described in. [76 77] Air permeability (in m^2) and apparent air flow resistance (in m^{-1}) of nanofibrous alumina sheets were determined according to Darcy's law [78] as $k_D=\mu hQ/(A\Delta P)$ and $R_D=h/k_D$, respectively, where h is the sheet (membrane) thickness in meters, Q is the air flow rate in m^3/s, A is the area in m^2, μ is the viscosity (1.78510–5 Pas for N2 at 25 oC), and ΔP is the pressure drop across the membrane (sheet).

Air permeability (Darcy's permeability parameter k_D) and apparent air flow resistance (R_D) were determined for several nanofibrous alumina single sheets and multilayer assemblies in order to evaluate their potential for the fabrication of filtration membranes and for other related applications. The results of these preliminary experiments are summarized in Fig. 15. The numbers for Darcy's permeability parameter were found within (1.5–3.0) $\times 10^{-13}$ m^2 for all tested nanofibrous structures with the membrane diameter of 5 mm, their thicknesses in the range from 40 to 360 μm, and calcined between 500 °C and 1000 °C. These numbers are comparable, on one hand, with the k_D reported for extruded porous alumina ceramics with unidirectionally aligned pores (10–40 μm pore size and >40% porosity) [77]. On the other hand, Fernando and Chung [76] reported 2–20 times larger k_D numbers for the fibrous membranes with the apparent mass density of 0.255 g/cm^3 and composed of 3-μm diameter alumina fibers, whereas Wiheeb et al [79] measured 2–4 times lower k_D for the membranes composed of a 9-μm mesoporous γ-alumina layer calcined at 600 °C on a macroporous α-alumina support sintered from powder at 1000 °C.

The observed initial decrease in the measured k_D magnitudes with the increase in pressure drop (Fig. 15a) across all tested nanofibrous alumina membranes can occur due to a partial compression of the membrane [80] and pore closure. Once a steady state was reached, the permeability of 700 ^{o}C and 1000 ^{o}C calcined membranes remained nearly constant until the membrane failed. A few kinks were observed in the permeability graphs of multilayer membranes. These kinks can occur as the result of sudden membrane deformation due to the relative sliding displacement of individual layers in the multilayer assembly, which could lead to macro-pore opening or closure. Such kinks were not observed in the single-sheet membranes, and it is not clear if they occur in 500 ^{o}C calcined multilayer assembly. The limited number of tests does not provide yet sufficient evidence for the interlayer slipping effect.

An increase in permeability above ΔP=10 kPa for the multilayer fibrous membrane calcined at 500 ^{o}C has been assigned to the membrane's partial stretching and increase of the distance between the fibers due to assumingly higher elasticity of this material. The shape of this membrane after the failure is consistent with the deformation of rather elastic fabric membranes. [81] The 500 ^{o}C calcined fibrous alumina membranes possessed also the lowest permeability and largest air flow resistance among the other tested structures. Both 700 ^{o}C and 1000 ^{o}C calcined single fibrous sheet membranes showed the same behavior of permeability and air flow resistance, as well as rather similar brittle failure features (Fig. 15b). Similar trends were also observed for the multilayer membranes. The lower k_D of 1000 ^{o}C calcined membranes was assigned to their denser structure when compared to 700 ^{o}C calcined ones (0.275 g/cm^3 *vs* 0.220 g/cm^3). The 700 ^{o}C calcined material had the

best overall performance (permeability 2.77×10^{-13} m^2 (or 0.28 Darcy), ΔP=47 kPa at failure).

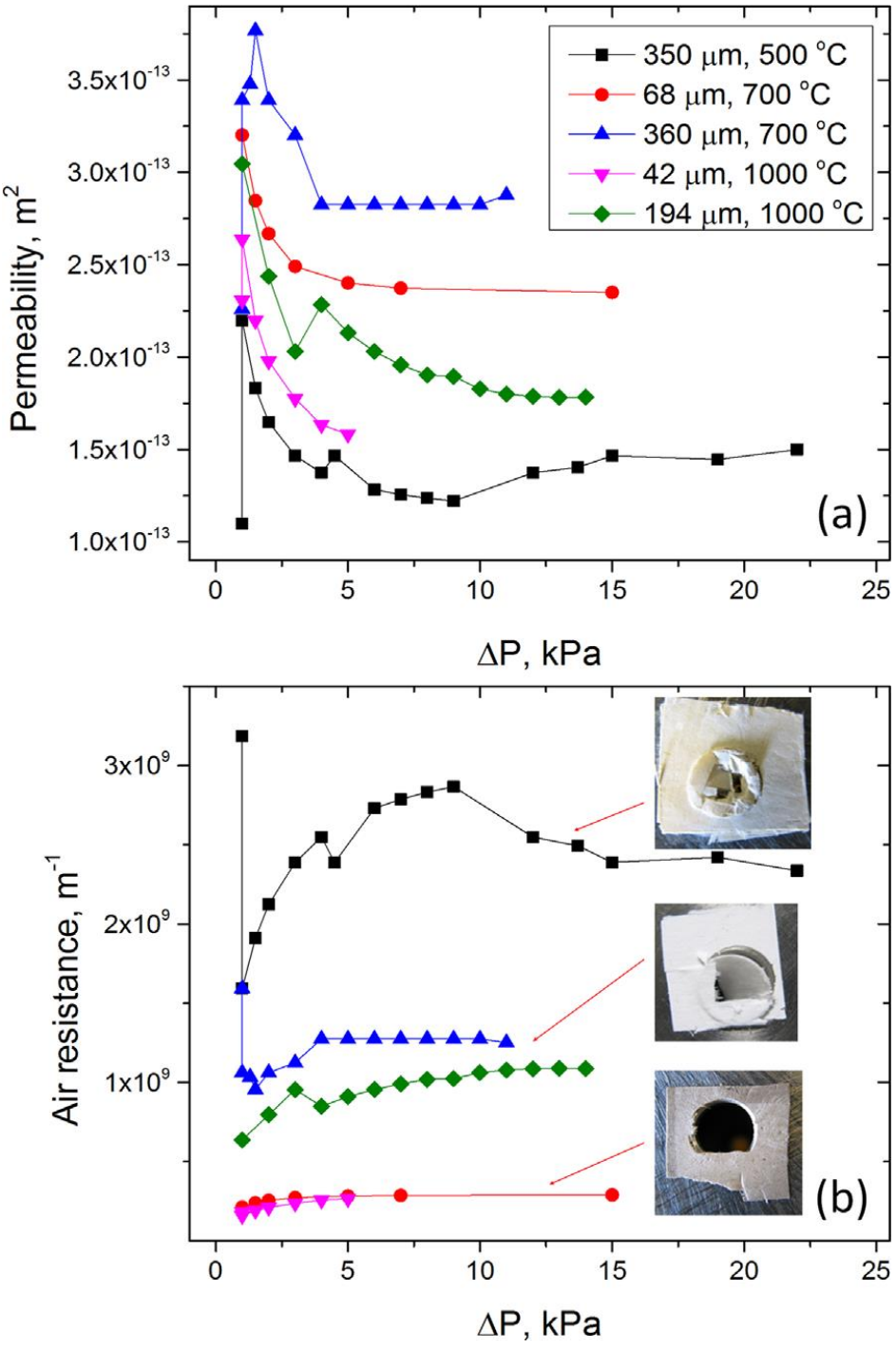

Figure 15. Permeability and air flow. Darcy's (a) permeability and (b) apparent air flow resistance of nanofibrous alumina sheets with different thickness calcined at 500, 700, and 1000 °C.

CHAPTER 6

CONCLUSIONS

Computational modeling of the electric field showed strong agreement with the experimental data. This model, however, can be further improved. With more time a model of greater complexity can be constructed. A more in-depth model that takes into account the “leaky dielectric” nature of the charged fluid and more complex shapes of electrodes is a goal of further research. Adding other phenonium such as moving charged particles in the electric field and the presence of coronal wind will further extend the model to help explain what happens in the flow at distances greater than a few centimeters away. Finally extending this computational to 3-dimensional space with nonsymmetrical electrodes is an intriguing yet unstudied investigation.

Nanocrystalline alumina (Al2O3) nanofibers, derived from 1:1 Al(NO3)3/PVP precursor fibers collected at the rates up to 6.4 g/h using a free-surface AC-electrospinning, exhibit the fiber diameter, surface morphology, and structure that to a certain extent are characteristic to alumina fibers produced from various precursors by other electrospinning methods. The formation of dense weakly charged fiber flows in AC-electrospinning method provides a capability for easier fiber handling and better fiber collection schemes.

AC-electrospun 100–300 μm thick single nanofibrous sheets and their multilayer assemblies were prepared and converted into nanofibrous γ-alumina structures using the

calcination temperatures between 700 and 1000 °C. The initial volume of calcined nanofibrous alumina single sheets shrunk 11–15 times, but little deformation and cracking was observed. Such volume shrinkage of fibrous structures appears to be proportional to that of individual nanofibers. However, the fiber shrinkage in radial and axial directions can be non-uniform due to the stress in precursor fibers determined by the voltage dependency of the organization of polymer molecules. Volume shrinkage of multilayer assemblies was 18–25 times, mostly due to the thickness reduction. Significant fiber bundling noted in AC-electrospinning, fiber collection procedure, inter-fiber interactions within the single sheet and multilayer fibrous assemblies during the compression, and the peculiarities of fiber shrinkage during calcination can define the final size, microarchitecture, and micro-/mesoporosity of the final structure, as well as its mechanical properties.

Air permeability and apparent air flow resistance parameters with the single sheet and multilayer nanofibrous alumina membranes were found comparable with porous alumina membranes of various designs and fabricated by different methods. This allows the nanofibrous alumina structures derived from AC-electrospun precursor fibers to be considered as a candidate material suitable for gas filtration and separation membranes, and other applications. The possibility of slipping between the layers in multilayer nanofibrous sheet assemblies and its effect on the mechanical properties and function of the structures are yet to be explored.

REFERENCES

1. Huang, Z.-M., A review on polymer nanofibers by electrospinning and. *Composites Science and Technology* **63**, 2223–2253 (2003).

2. Suthat A, C. G. *Chemical Engineer*, 26-28 (2001).

3. Chronakis, I. S., Novel nanocomposites and nanoceramics based on polymer nanofibers. *Journal of Materials Processing Technology* **167**, 283–293 (2005).

4. Taylor, G. I., Electrically driven jets. *Proceedings of the Royal Society of London A* **313**, 453 (1969).

5. Taylor, J. R. M. a. G. I., Electrohydrodynamics: A review of the role of inerfacial stresses. *Annu. Rev. of Fluid Mech* **1**, 111 (1969).

6. Moses M. Hohman, M. S. G. R. M. P. B., Electrospinning and electrically forced jets. I. Stability theory. *Physics of Fluids* **13** (2001).

7. Saville, D. A., Electrohydrodynamics: The Taylor-Melcher leaky dielectric model. *Annual Review of Fluid Mechanics* **29**, 27 (1997).

8. Saville, D. A., Electrohydrodynamics stability: Fluid cylinders in longitudinal electric fields. *Phys. Fluids* **13**, 2987 (1970).

9. Saville, D. A., Stability of electrically charged viscous cylinders. *Phys. Fluid Mech.* **49**, 361 (1970).

10. Mestel, A. J., Electrohydrodynamic stability of a slightly viscous jet. *J. Fluid Mech.* **274**, 93 (1994).

11. J. M. Lopez-Herrera, A. M. G.-C. a. M. P.-S., One dimensional simulation of the breakup of capillary jets of conducting liquids: Applications to e.h.d. spraying. *J. Aerosol Sci* **30**, 895 (1999).

12. C. J. Luo, S. D. S. E. S. E. P. a. M. E., Electrospinning versus fibre production methods: from specifics to technological convergence. *Chem Soc Rev* **41**, 4708-4735 (2012).

13. X.B. Ke, H. Y. Z. X. P. G. J. W. L. Z. F. Z., High performance membranes with a seperation layer of metal oxide nanofibers. *Adv. Mater.* **19**, 785-790 (2007).

14. Y.Dai, W. L. F. S. X., Ceramic nanofibers fabricated by electrospinning and and their application in cataylsis, enviornmental science, and energy technology. *Polym. Adv. Technol.* **22**, 326-338 (2001).

15. D. Malwal, P. G., Fabrication and applications of ceramic nanofibers in water remediation: A review. *Crit. Rev. Environ. Sci. Technol.* **46**, 500-534 (2016).

16. M. Büyükyazi, S. M., 3D nanoarchitectures of α-LiFeO2 and α-LiFeO2/C nanofibers for high power lithium-ion batteries. *Nano Energy* **13**, 28-35 (2015).

17. A. Nikfarjam, N. S., Improvement in gas-sensing properties of TiO2 nanofiber sensor by UV irradiation. *Sensors and Actuators B: Chemical* **211**, 146-156 (2015).

18. A.Sedaghat, E. T.-N. N., An alumina mat with a nano microstructure prepared by centrifugal spinning method. *Journal of Non-Crystalline Solids* **352**, 2818-2828 (2006).

19. A. Biswas, H. P. W. M. S., Flexible ceramic nanofibermat electrospun from TiO2–SiO2 aqueous sol. *Ceramics International* **38**, 883-886 (2012).

20. Y. Si, X. M. H. Z. J. Y. B. D., Silica nanofibrous membranes with ultra-softness and enhanced tensile strength for thermal insulation. *RSC Adv.* **5**, 6027-6032 (2015).

21. L. Ren, R. O. P. K., Rapid and efficient fabrication of multilevel structured silica micro-/nanofibers by centrifugal jet spinning. *Journal of Colloid and Interface Science* **425**, 136-142 (2014).

22. E. Formo, M. S. Y. E. P. L. L. L. Y. X., Functionalization of electrospun ceramic nanofibre membranes with noble-metal nanostructures for catalytic applications. *J. Mater. Chem.* **19**, 3878-3882 (2009).

23. V. Su, M. T. C., Filtration Performance of Membranes Produced Using Nanoscale Alumina Fibers (NAF). *Adv. Eng. Mater.* **14**, 1088-1096 (2012).

24. M. Vahtrus, M. U. B. P. L. D. R. S. M. T. K. S., Mechanical and structural characterizations of gamma- and alpha-alumina nanofibers. *Materials Characterization* **107**, 119-124 (2015).

25. Y. Wang, W. L. Y. X. X. J. C., Electrospun flexible self-standing γ-alumina fibrous membranes and their potential as high-efficiency fine particulate filtration media. *Journal of Materials Chemistry A* **2**, 15124-15131 (2014).

26. P.K. Panda, S. R., Electrospinning of alumina nanofibers using different precursors. *J. Mater. Sci.* **42**, 2189-2193 (2007).

27. E. Carneiro, P. S. B. A. C. A. P. J. T. F. J. P. M., Effect of electrospun alumina nanofibers incorporation in ceramic glaze. *J. Ceram. Sci. Technol* **6**, 69-74 (2015).

28. P.C. Yu, R. J. Y. Y. Y. T. W. S. F. S. Y., Growth mechanism of single-crystal α-Al2O3 nanofibers fabricated by electrospinning techniques. *Journal of the European Ceramic Society* **31**, 723-731 (2011).

29. M.M. Dimitrova, E. D. K. D. B. K., Simplified procedure for Al2O3 microfibers preparation by the method of electrospinning. *Bul. Chem. Comm.* **45**, 94-98 (2013).

30. S. Zhang, X. Y. C. Y. M. M., Fabrication of alumina ribbons with mixed solvent system in electrospinning. *Journal of Optoelectronics and Advanced Materials* **13**, 425-427 (2011).

31. XueyuanTang, Y. Y., Electrospinning preparation and charactorization of alumina nanofibers with high aspect ratio. *Ceramics International* **41**, 9232-9238 (2015).

32. Chandradass, B., Sol-Gel processing of alumina fibers. *J. Mater. Process. Technol.* **173**, 275-280 (2006).

33. Azad, A. M., Fabrication of transparent alumina nanofibers by electrospinning. *Material Sci. Engineer. A.*, 435-436 (2006).

34. Sarawati, R. R. R., Structural evolution in alumina gel. *J. Msater. Sci.* **22**, 2529 (1987).

35. Fernando, C., Thermochemical properties of alumina memrane. *Ceramics International* **31**, 453 (2005).

36. Y.Wang, W. L. X. J. D. C., Electrospinning preparation and adsorption properties of mesoporous alumina fibers. *J. Mater. Chem. A* **1**, 10720-10726 (2013).

37. H. Niu, T. L., Fiber generators in needleless electrospinni. *J. Nanomat.* **2012** (2012).

38. T. Miloh, B. S. A. L. Y., Needleless electrospinning: Electrically driven instability and multiple jetting from the free surface of a spherical liquid layer. *J. Appl. Phys.* **106** (2009).

39. D. Lukas, A. S. P. P., Self organization of jets in electrospinning from free liquid surface: A generalized approach. *J. Appl. Phys* **103** (2008).

40. M. Shin, M. M. H. M. P. B. C. R., Electrospinning: A whipping fluid jet generates submicron polymer fibers. *Appl. Phys. Lett* **78**, 1149 (2001).

41. Azad, A. M., Fabrication of transparent alumina nanofibers by electrospinning. *Mater. Sci.* **468**, 435-436 (2006).

42. M. Yanilmaz, Y. L. J. Z. X. Z., Silica/polyacrylonitrile hybrid nanofiber membrane separators via sol-gel and electrospinning techniques for lithium-ion batteries. *J. Power Sources* **313**, 205-212 (2016).

43. H.T. Chiu, T. S. M. T. K. Y. H. W. K. W., Surface modification of aluminum nitride by polysilazane and its polymer-derived amorphous silicon oxycarbide ceramic for the enhancement of thermal conductivity in silicone rubber composite. *Appl. Surf. Sci.* **292**, 928-936 (2014).

44. Soshana A. Smitha, B. P. W. Y. L. J., Effect of polymer and ceramic morphology on the material and. *J. Mem. Sci* **526**, 315-322 (2017).

45. Demir MM, Y. I. Y. E. E. B., Electrospinning of polyurethane fibers. *Polymer* **43**, 3303-3309 (2002).

46. Fong H, C. I. R. D., Beaded nanofibers formed during electrospinning. *Polymer* **40**, 4585-4592 (1999).

47. PK, B., Electrostatic spinning of acrylic microfibers. *J. of Colloid and Interface Science* **36**, 71-79 (1971).

48. Doshi J, R. D., Electrospinning process and applications of electrospun fibers. *J. Electrostatics* **35**, 151-160 (1995).

49. Deitzel JM, K. J. H. D. T. N., The effect of processing variables on the morphology of electrospun nanofibers and textiles. *Polymer* **42**, 261-272 (2001).

50. P.Pokorny, E. K. S. M. C. K. B. *Phys.Chem.Chem.Phys.* **16**, 26816–26822 (2014).

51. C. Lawson, A. S. S. P. L., Rapid fabrication of poly(ε-caprolactone) fibers using needleless alternating current electrospinning. *J. Appl. Polym. Sci.* **133**, 43232 (2016).

52. A.M. Drews, L. C. G. M. W. K. J. M. B. *J. Appl. Phys.* **114**, 143402 (2012).

53. Goldstein, G. I. *et al.*, Scanning electron microscopy and x-ray microanalysis. *Plenum Press* (1981).

54. Suzuki, E., High-resolution scanning electron microscopy of immunogold-labelled cells by the use of thin plasma coating of osmium. *J. Microscopy* **208**, 153-157 (2002).

55. Frank, A., The Cambridge Structural Database: a Quarter of a Million Crystal Structures and Rising. *Acta Crystallographica Section B* **58**, 380-388 (2002).

56. Griffiths, P. R. & Haseth, J. A. D., *Fourier Transform Infrared Spectrometry*, 2nd ed. (John Wiley & Sons, 2007).

57. Brault, J. W., New Approach to high-precision Fourier transform spectrometer design. *Appl. Optics* **35**, 2891-2896 (1996).

58. Askeland, D. R. & Phulé, P. P., *The Science and Engineering of materials*, 5th ed. (Cengage Learning, 2006).

59. Niu, L., Using the Bending Beam Model to Estimate the Elasticity of Diphenylalanine Nanotubes. *Langmuir* **23**, 7443-7446 (2007).

60. F.O. Ochanda, M. A. S. H. V. T. G. C. T. M. G.-E.-H., Fabrication of superhydrophobic fiber coatings by DC-biased AC-electrospinning. *J. Appl. Polymer Sci.* **123**, 1112-1119 (2012).

61. S. Sarkar, S. D. G. T., Biased AC electrospinning of aligned polymer nanofibers. *Macromolecular Rapid Comm.* **28**, 1034-1039 (2007).

62. R. Kessick, J. F. G. T., , The use of AC potentials in electrospraying and electrospinning processes. *Polymer* **45**, 2981-2984 (2004).

63. S. Maheshwari, H. C. C., Assembly of multi-stranded nanofiber threads through AC electrospinning. *Adv. Mater* **21**, 349-354 (2009).

64. A. Stanishevsky, J. W. M. W. I. S. H. Y.-L., Ribbon-like structures of tungsten oxide nanofibers. *RCS Adv.* **5**, 69534-69542 (2015).

65. B. Pacewska, M. K., Thermal transformations of aluminium nitrate hydrate. *Thermochim. Acta* **385**, 73-80 (2002).

66. ICDD, S. K. E., Powder Diffraction File (2007).

67. Cullity, B. D., Elements of XRD, 2nd ed. *Addison-Wesley, Reading, MA, USA,* (1978).

68. Saniger, J. M., Al-O infrared vibrational frequencies of γ-alumina. *Mater. Lett.* **22**, 109-113 (1995).

69. J.H. Kim, S. J. Y. D. H. K. H. J. J. T. Y. K. K. H. P. J. W. L., Characterization and application of electrospun alumina nanofibers. *Nanoscale Res. Lett* **9**, 44-49 (2014).

70. S.Y. Reyes-López, R. S. A. R. L.-J. J. S. R., Analysis of the phase transformation of aluminum formate AL(O2CH)3 to α-alumina by Raman and infrared spectroscopy. *J. Ceram. Proc. Res* **14**, 627-631 (2013).

71. L. Favaro, A. B. P. R. J. L. G. S. J. B. B. A. M. H. R. T., Experimental and ab initio infrared study of χ-, κ- and α-aluminas formed from gibbsite. *J. Solid State Chem* **183**, 901-908 (2010).

72. P.Liu, Y. Z. M. Y. G. X., Preparation of continuous porous alumina nanofibers with hollow structure by single capillary electrospinning. *Colloids Surf.A: Physicochem. Eng. Asp.* **436**, 489-494 (2013).

73. A. Mahapatra, B. G. M. G. H., Synthesis of ultra-fine α-Al2O3 fibers via electrospinning method. *Ceram. Int.* **37**, 2329-2333 (2011).

74. Z. Saunders, C. W. N. A. D. V. L., Characterization of engineered aluminana nofibers andt heir colloidal properties in water. *J. Nanopart. Res.* **17**, 140-153 (2015).

75. H. Fan, C. H. T. B. D. T. R. A. R. S. D. J. K. D. J. L. S. T. C. J. B., Modulus–density scaling behaviour and framework architecture of nanoporous self-assembled silicas. *Nature Materials* **6**, 418-423 (2007).

76. J.A. Fernando, D. D. L. C., Pore structure and permeability of an alumina fiber filter membrane for hot gas filtration. *J. Porous Mater* **9**, 211-219 (2002).

77. T. Isobe, Y. K. A. N. K. O. Y. H., Gas permeability and mechanical properties of porous alumina ceramics with unidirectionally aligned pores. *J. Eur. Ceram. Soc.* **27**, 53-59 (2007).

78. Dullien, F., Porous Media – Fluid Transport and Pore Structure. *Academic Press New York*, 157 (1979).

79. A.D.Wiheeb, M. A. A. N. M. K. R. O., Identification of molecular transport mechanisms in micro-porous hydrotalcite–silica membrane. *Transp. Porous Med.* **104**, 133-144 (2014).

80. L.T. Choong, Z. K. G. C. R., Permeability of electrospun fiber mats under hydraulic flow. *J. Membr. Sci.* **451**, 133-144 (2014).

81. P.W. Gibson, K. D. T. G., Dynamic permeability of porous elastic fabrics. *J. Eng. Fabr* **7** (Special issue), 29-36 (2012).

82. Hulteen, J. C., A general tamplate-based method for the preparation of nanomaterials. *J. Mater. Chem.* **7**, 1075 (1997).

83. Noordin, L., Synthesis of Alumina Nanofibers and compoites. *Nanofibers* (2010).

84. Choi, K. M. L., Preperation and characterization of ultra thin alumina hollow fiber microfiltration membrane. *Desalination* **193**, 256 (2006).